RSC Advances

PAPER

View Article Online
View Journal | View Issue

Cite this: *RSC Adv.*, 2026, **16**, 1368

2D assembled $ZnO/ZnCo_2O_4$ heterostructures as efficient electrocatalysts for electrochemical detection of ofloxacin in water: experimental and DFT study

Vu Thi Huong Mai,†[a] Ngoc Huyen Nguyen, †[a] Nguyen Thanh Vinh,[b] Tran Vinh Hoang,[c] Le Minh Tung,[d] Manh-Huong Phan,[e] Anh-Tuan Le[a] and Ngo Xuan Dinh *[a]

In this work, assembled $ZnO/ZnCo_2O_4$ heterostructure nanosheets (ZnO/ZCO) were successfully synthesized through a rapid one-step microwave-assisted hydrothermal method. The $ZnO/ZnCo_2O_4$ sample features an ordered assembly of nanocrystals with a size of 30 nm forming two dimensional (2D) nanosheets, and $ZnO\text{-}ZnCo_2O_4$ heterojunctions are uniformly distributed. The physicochemical properties of ZnO/ZCO heterostructures were systematically studied by combining experiments and density functional theory (DFT) calculation. The heterojunction configuration of ZnO and $ZnCo_2O_4$ produced an interfacial charge redistribution and strong electronic interaction, resulting in the enhanced electrocatalytic performance towards ofloxacin (OFL). Consequently, the $ZnO/ZnCo_2O_4$ heterostructure nanosheet-based electrochemical sensor possessed an outstanding sensing performance in the detection of OFL with a high electrochemical sensitivity of 1.97 $\mu A\ \mu M^{-1}\ cm^{-2}$. In addition, the proposed sensor was successfully applied for the detection of OFL in tap and lake water with recovery rates of 97.0–99.2%. The study demonstrates the potential of spinel oxide-based electrochemical sensors for rapid and cost-effective detection of antibiotic residues, providing an effective solution for water quality safety monitoring.

Received 19th November 2025
Accepted 23rd December 2025

DOI: 10.1039/d5ra08937a

rsc.li/rsc-advances

1. Introduction

Antimicrobial resistance associated with antibiotic residues in the environment has been recognized as one of the greatest threats to global health.[1] Due to widespread and injudicious usage of antibiotics in the treatment of human infectious disease, livestock industry, and aquaculture, the non-metabolized antibiotics and their residues will be discharged into the natural water environment, resulting in antibiotic pollution. Concern over the growing antibiotic pollution issues has promoted the development of sensing techniques in the monitoring of antibiotic residues to ensure the safety and cleanliness of water environments. Ofloxacin (OFL), a synthetic antibiotic belonging to the quinolone class, has a broad-spectrum antibacterial activity against both Gram-negative bacteria and Gram-positive bacteria.[2–5] OFL is often abused in medicine, aquaculture, and livestock industries due to its low cost and importance in preventing and treating various bacterial infectious diseases, leading to its excessive residue in food and the environment. In addition, OFL is difficult to biodegrade owing to its antibacterial action on beneficial microorganisms that assist wastewater treatment, resulting in the rising OFL accumulation in the environment. Therefore, it is urgent to develop an efficient analytical technique for monitoring and preventing the accumulation of OFL amount in aqueous environments.

Traditionally, analytical techniques such as liquid chromatography-tandem mass spectrometry (LC/MS/MS),[6] high-performance liquid chromatography (HPLC),[7] and capillary electrophoresis[8] are used to monitor the OFL amounts in the environment. These analytical techniques require high costs, sophisticated instruments, complex operations, time-consuming sampling, and well-qualified operators. Electrochemical sensing strategies have been recognized as an attractive solution for developing a sensing system with high mobility and sensitivity, enabling the online monitoring and on-site

[a]*Phenikaa University Nano Institute (PHENA), Phenikaa University, Hanoi 12116, Vietnam*

[b]*University of Transport Technology, Hanoi 12116, Vietnam. E-mail: dinh.ngoxuan@phenikaa-uni.edu.vn*

[c]*School of Chemistry and Life Science, Hanoi University of Science and Technology, 1st Dai Co Viet Road, Hanoi 10000, Vietnam*

[d]*Department of Physics, Tien Giang University, Dong Thap City, Vietnam*

[e]*Center for Materials Innovation and Technology (CMIT), VinUniversity, Gia Lam District, Hanoi 10000, Vietnam*

† Equal contribution.

detection of antibiotic residue.[9,10] Moreover, the customized modification of working electrode surface with nanomaterials allows the development of selective and sensitive electrochemical sensors that are fully operational in real conditions.[11] Nanomaterials can significantly improve the electrochemical sensor performance by providing a high surface-to-volume ratio, rapid electron transfer, and superior electrocatalytic activity.[12,13] A large variety of nanostructures such as carbon nanotubes, metal–organic frameworks (MOFs),[14] metal oxides,[15] and graphene oxide[16] have developed as electrochemical sensing platforms for detection of OFL. Spinel oxides and their nanocomposites have attracted great attention as excellent electrocatalysts for electrochemical sensing applications owing to their low cost, multiple oxidation states, and stability.[17,18] Solangi *et al.*[19] developed the $NiCo_2O_4$ nanoboulders with strong electrochemical activity as electrode material for detection of OFL. Liao *et al.*[20] developed a electrocatalytic platform through the *in situ* growth of Fe_3O_4 nanoparticles on N-doped hollow carbon spheres for electrochemical sensing of OFL in water. The combination of Fe_3O_4 nanoparticles and N-doped hollow carbon spheres enhances the overall electron transfer capability of the N-HCS/Fe_3O_4 nanocomposites. JS de Castro *et al.*[21] developed an electrocatalytic amplified sensor using Zn_2SnO_4/reduced graphene oxide composite for detection of OFL. However, for a given analyte, the sensing performance significantly depends on the nanostructured modifiers that is precisely designed for selective signal amplification towards the target analyte.[12,13] For a direct electrochemical detection of OFL, the key factors affecting the electrochemical sensor performance are the electrocatalytic activity and electron transfer efficiency of electrode material.[11] Therefore, the development of cost-effective electrocatalysts with rapid electron transfer and a high electrocatalytic activity for electrochemical detection of OFL is of great research and environmental safety.

In recent years, the construction of heterostructures by combining two semiconductors with different band gaps has been a promising strategy for enhancing the electrochemical sensing performance by boosting the electron transfer efficiency and electrocatalytic activity at interface·[22–24] In particular, the p–n heterojunction formation would induce a strong built-in electric field, which can regulate the electronic structure of nearby components.[25] In addition, the formation of built-in electric field also promotes spatial charge carrier migration and inhibits electron-hole recombination, resulting in an enhancement of sensor performance.[26] Recently, Song *et al.*[27] developed a photoelectrochemical (PEC) aptasensor using a CdS/Cu_2MoS_4 Z-type heterojunction for determination of OFL in water. The CdS/Cu_2MoS_4 Z-type heterojunction significantly inhibits electron-hole complexation, which significantly increases photocurrent intensity of the system. Zinc cobaltite ($ZnCo_2O_4$), a typical p-type semiconductor, is an excellent cobalt-based ternary metal oxide for applications in the electrochemical sensing field because of its favorable electrochemical properties.[28–30] In the n-type semiconductors, ZnO has attracted considerable attention due to its commendable properties such as low cost, high electron communication features, and electrochemical activities.[31] In addition, ZnO crystalline phase has excellent interfacial compatibility with $ZnCo_2O_4$ phase and contributes to the construction of stable and efficient heterojunction structures.[32] The porous spherical $ZnCo_2O_4$/ZnO was developed for the gas semiconductor sensor to detect butanone with high sensitivity.[33] The $ZnCo_2O_4$ can regulate the electronic structure of ZnO surface, reducing the HOMO–LUMO gap favorably to promote the reaction with butanone.[33] Currently, the microstructure and physical properties of heterostructures could be inferred based on the first principle calculation, thereby improving the electrocatalytic activity and providing reliable guidance for targeted design and optimization of sensing performance.[34,35] The density functional theory (DFT) calculations and experimental results proved that the existence of built-in electric field in ZnO/$ZnCo_2O_4$ heterojunction promoted charge transfer and ions diffusion.[36] Ma *et al.*[37] designed the ZnO/$ZnCo_2O_4$ heterostructure by combining DFT simulations and purposely designed experimental studies for improving the photocatalytic CO_2 reduction. Therefore, the design and construction of ZnO/$ZnCo_2O_4$ heterostructure with a high electrocatalytic activity by combining DFT calculations and experiments would be a promising strategy for the on-site monitoring of OFL.

The microwave-assisted hydrothermal strategies enable regulation of the heterojunction interface and controlling the component uniformity, which can obtain a more uniform and compact structure. This work presents a rapid synthesis of ZnO/$ZnCo_2O_4$ heterojunction with unique two-dimensional (2D) nanostructure assembled by uniform nanoparticles *via* a microwave-assisted hydrothermal approach. The high electrocatalytic activity and rapid electron transfer of ZnO/$ZnCo_2O_4$ heterostructures are speculated and validated by combining experimental and theoretical studies. With electrocatalytic activity and electron transfer promotion, ZnO/$ZnCo_2O_4$ heterostructures show an excellent electrocatalyst towards OFL, thereby facilitating on-site monitoring and detection of antibiotic residue. The application of the electrochemical sensor based on 2D ZnO/$ZnCo_2O_4$ nanosheets for detection of OFL in the environmental samples was tested.

2. Experimental section

2.1. Reagents and apparatus

Zinc nitrate hexahydrate ($Zn(NO_3)_2 \cdot 6H_2O$), cobalt(II) nitrate hexahydrate ($Co(NO_3)_2 \cdot 6H_2O$), $K_3[Fe(CN)_6]$, urea ($(NH_2)_2CO$), and $K_4[Fe(CN)_6]$ were provided from Xilong Scientific Co., Ltd (China). NaOH and HCl were purchared from Ducgiang Chemical JSC, Vietnam. Carbon screen-printed electrode (SPE) was purchared from Metrohm Co., Ltd (Vietnam). All the chemicals were used without any further purification.

The crystalline microstructure of as-prepared samples was characterized using a Bruker D5005 X-ray Diffractometer (Germany). The X-ray diffraction (XRD) patterns were analyzed by the Rietveld refinement using the Fullprof program. Field emission scanning electron microscopy (FE-SEM, Regulus 8100, Hitachi) equipped an energy-dispersive X-ray spectrometer was used to investigate the surface morphology and composition of as-prepared samples. The Raman spectra were carried out on

a MacroRam spectroscopy (Horiba Scientific) using a 785 nm laser source. The various pH solutions were prepared by using NaOH and HCl solutions, and examied by a LAQUA pH1200 meter (Horiba, Japan).

2.2. Synthesis of the ZnO/ZCO nanosheets

ZnO/ZCO nanosheets were successfully synthesized by using a microwave-assisted hydrothermal method. In a typical procedure, 7.5 mmol of $Zn(NO_3)_2 \cdot 6H_2O$, 5 mmol of $Co(NO_3)_2 \cdot 6H_2O$ and 60 mmol of urea were orderly dissolved in 300 ml deionized (DI) water. Then, as-prepared solution was loaded into a 500 ml Teflon-lined autoclave in a UWave-2000 microwave reactor system (SINEO, China), and heated at 160 °C for 5 minutes with a power setting of 600 W. The purple precipitates were collected by centrifugation, washed with DI water and ethanol, and dried at 80 °C for 12 h. In the end, the dried powders were annealed at 400 °C for 2 h to obtain the ZnO/$ZnCo_2O_4$ heterojunction.

2.3. Preparation of ZnO/ZCO/SPE electrodes and electrochemical response studies

The purchased-SPEs were rinsed with DI water and dried for 1 h at 35 °C. 10 mg of ZnO/ZCO sample was dispersed sonochemically in 10 ml of DI water for 1 h to obtain the well-dispersed ZnO/ZCO suspension. Then, 6 μl of ZnO/ZCO suspension was used to modify the surface of SPEs *via* a simple drop-casting method, and dried at 40 °C for 2 h. For comparison, similar procedure is used to prepare $ZnCo_2O_4$/SPE electrode.

The cyclic voltammetry (CV) experiments were recorded in 0.1 M KCl solution containing 2.5 mM $K_3[Fe(CN)_6]$ and 2.5 mM $K_4[Fe(CN)_6]$ in the potential range from −0.3 V to 0.6 V at various scan rates of 10–60 mV s^{-1}. The electrochemical impedance spectroscopy (EIS) experiments was performed in a frequency range of 0.01–50 000 Hz with E_{ac} = 10 mV, E_{dc} = 0.15 V. The Mott–Schottky (MS) measurements were performed at 1 kHz using 0.1 M Na_2SO_4 solution as electrolyte with scanning potential in the range from −1.0 V to 1.0 V. The electrochemical kinetic parameters of modified electrodes were investigated by CV experiments in 0.1 M PBS solution containing 100 μM OFL. The chronoamperometry (CA) experiments were carried out at the potential of 960 mV in 0.1 M PBS solution containing of various OFL concentrations (0, 10, 25, and 100 μM). Differential pulse voltammetry (DPV) was carried out in the potential range of 0.4 V and 1.0 V in 0.1 M PBS solution containing a certain concentration of OFL with a pulse with of 0.25 s, a pulse height of 50 mV, a step potential of 5 mV, and a scan rate of 0.006 V s^{-1}. All electrochemical tests were carried out on an electrochemical workstation (PalmSens4) at room temperature.

2.4. Theoretical calculations

All theoretical calculations were carried out using Dmol3 and CASTEP modules included in Materials Studio Software (BIOVIA Materials Studio). The model of ZnO/$ZnCo_2O_4$ heterostructures was built based on the ZnO (001) crystal plane and $ZnCo_2O_4$ (001) crystal plane with a mismatch rate of 13% and a vacuum region of 15 Å. The geometry optimization and density of states (PDOS and TDOS) were calculated using Dmol3 module with the generalized gradient approximation (GGA) functional of the Perdew–Wang exchange and correlation functional (PW91). The calculations adopted a double numerical basis with polarization functions (DNP) to describe electrons and nuclear interaction. The convergence tolerance of energy, maximum force, maximum displacement are set to 1.0×10^{-5} Ha, 0.002 Ha $Å^{-1}$ and 0.005 Å, respectively. The maximum iterations and maximum step size are 50 and 0.3 Å. The Brillouin zone was sampled by a 4 × 4 × 1 uniform k point mesh for geometry optimization. The optimized lattice constants of ZnO/$ZnCo_2O_4$ heterostructures are found to be $a = b = 6.10$ Å, $c = 21.78$ Å, and $\alpha = \beta = 90°$, $\gamma = 105°$. The electron density difference and electron localization function are calculated by using the CASTEP module with the generalized gradient approximation (GGA) functional of the Perdew–Wang exchange and correlation functional (PW91) based on the optimized ZnO/$ZnCo_2O_4$ heterostructures. The energy cutoff, SCF (Self-Consistent Field) tolerance, and SCF maximum are 489.8 eV, 10^{-5} eV per atom, and 100. The adsorption of OFL on the ZCO and ZnO/ZCO was simulated by using Adsorption Locator tool in Materials Studio. The model of surface was simulated by the (011) crystal plane of ZCO and ZnO/ZCO with (3 × 3) layers and a 15 Å vacuum region.

3. Results and discussion

3.1. Morphological and structural characterization of ZnO/$ZnCo_2O_4$ heterostructures

The crystal microstructure and phase composition of ZnO/$ZnCo_2O_4$ sample were determined by X-ray diffraction analysis. XRD pattern and Rietveld refinement with Bragg positions of ZnO and $ZnCo_2O_4$ phases are depicted in Fig. 1a. The diffraction peaks at 18.7°; 31.5°; 36.2°; 44.4°; 55.1°; 58.8° and 64.7° can be indexed to the (111); (220); (311); (400); (422); (511) and (440) crystal planes of $ZnCo_2O_4$ spinel phase (JCPDS 23-1390). The other diffraction peaks at 30.7°; 34.1°; 47.4°; 56.5°; 62.6° and 68.0° can be assigned to the (100); (002); (102); (110); (103), and (112) crystal planes of ZnO phase (JCPDS 36-1451). No other impurities are observed in the prepared sample, confirming the formation of heterostructures from two ZnO and $ZnCo_2O_4$ phases. Rietveld refinement was performed by a Fullprof suite software to provide the detail structural information of ZnO and $ZnCo_2O_4$ phases in the prepared sample. The refinement is good reliability ($\chi^2 = 1.43$) with low R-factors ($R_{wp} = 6.66$, and $R_{exp} = 5.58$), and the obtained parameters are listed in Table S1. The analysis results confirm $ZnCo_2O_4$ crystalline in the cubic spinel structure ($Fd3m$) where the tetrahedral sites are fully occupied by Zn ions and all Co ions are filled in the octahedral sites. The ZnO phase belongs to the hexagonal wurtzite structure system with space group $P6_3mc$. The obtained lattice parameters are $a = b = 3.26$ Å, $c = 5.24$ Å, and $a = b = c = 8.15$ Å for ZnO and $ZnCo_2O_4$ phases, respectively. In addition, the quality percentages of ZnO and $ZnCo_2O_4$ phases were calculated to be 38.5% and 61.5% from the Rietveld refinement data, respectively. Fig. 1b and c show SEM images of ZnO/$ZnCo_2O_4$

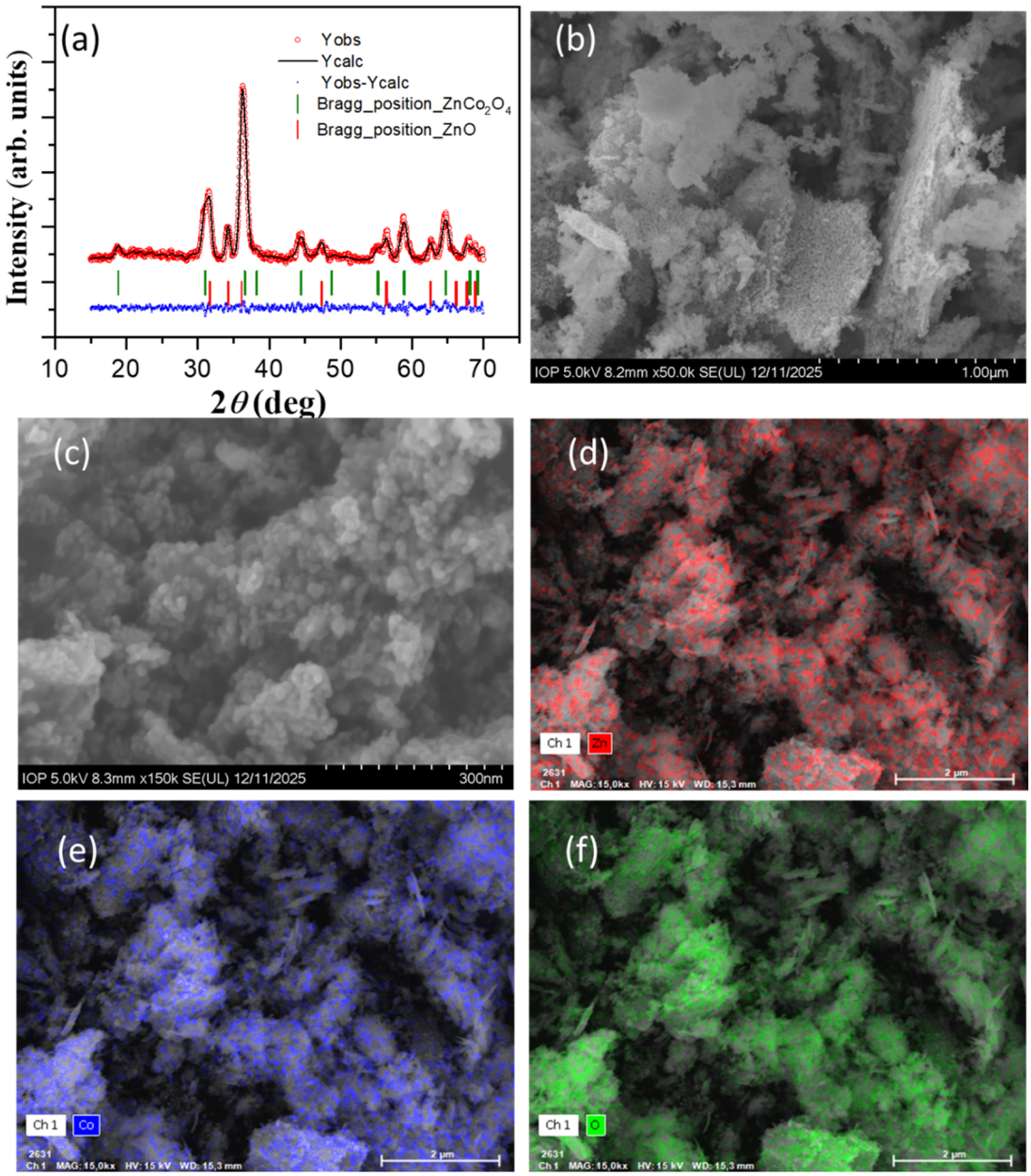

Fig. 1 (a) X-ray, (b and c) FE-SEM, and (d–f) EDX elemental mapping images of ZnO/$ZnCo_2O_4$ heterostructures.

heterostructures. It can be observed that ZnO/ZCO sample exhibits nanosheets (2D) assembled by uniform nanoparticles with a size of about 15–20 nm. The EDX elemental mapping images of ZnO/$ZnCo_2O_4$ heterostructures confirm the presence of Zn, Co and O signals (Fig. 1d–f). It can be seen that the Zn, Co and O atoms are uniformly distributed. The EDX analysis result shows that the atomic percentages of Zn, Co, and O are 25.84%, 14.52%, and 59.46%, respectively. These results further confirm the formation of ZnO/$ZnCo_2O_4$ heterostructures.

The Raman spectroscopy is a powerful technique, which can provide unique information of nanostructured transition metal oxides. The Raman spectrum of ZnO/$ZnCo_2O_4$ heterostructures shows five characteristic bands at 197 cm^{-1}, 490 cm^{-1}, 530 cm^{-1}, 630 cm^{-1}, and 680 cm^{-1}, which are assigned to F_{2g}, E_g, F_{2g}, F_{2g} and A_{1g} vibrational modes of $ZnCo_2O_4$, respectively.[38] The other bands at 432 cm^{-1} and 570 cm^{-1} are ascribed to E_{2H} and A_{1L} vibrational mode of ZnO, confirming the presence of hexagonal wurtzite ZnO[39,40] (Fig. 2).

The heterostructures and electrical characterization of ZnO/$ZnCo_2O_4$ sample were characterized by Mott–Schottky analysis. The Mott–Schottky plots of $ZnCo_2O_4$ and ZnO/$ZnCo_2O_4$ samples in 0.1 M Na_2SO_4 solution with a frequency of 1 kHz in are shown in Fig. 3. For $ZnCo_2O_4$ sample, the Mott–Schottky plot shows a negative slope, indicating the p-type of semiconductor characteristic of $ZnCo_2O_4$. The flat band potential (V_{fb}) of $ZnCo_2O_4$ is approximated about 1.07 V (*vs.* Ag/AgCl). Notably, the Mott–Schottky plot of ZnO/$ZnCo_2O_4$ heterostructure exhibits a clear inverted "V" shape with both negative and positive slopes,

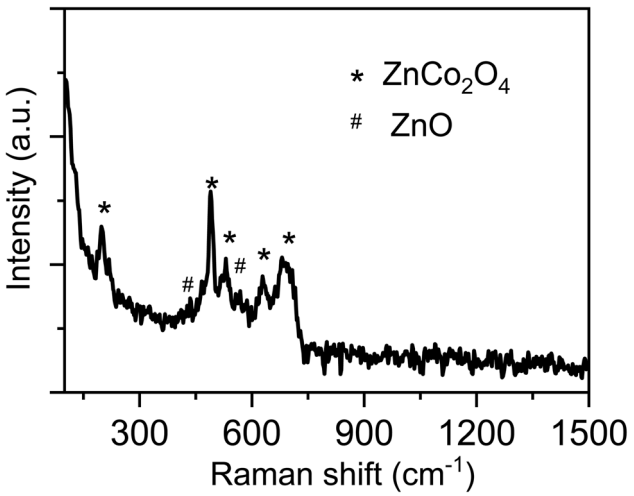

Fig. 2 Raman spectrum of $ZnO/ZnCo_2O_4$ heterostructures.

confirming the formation of p–n heterojunction between ZnO and $ZnCo_2O_4$. The V_{fb} value is calculated to be about 1.38 V (*vs.* Ag/AgCl) for $ZnO/ZnCo_2O_4$ heterostructure. The shift of V_{fb} value can be attributed to the passivation of surface states by forming heterojunction that suppress the Fermi-level pinning.[41] In addition, the acceptor density (N_A) of $ZnCo_2O_4$ and $ZnO/ZnCo_2O_4$ can be calculated by using following equation:[42]

$$N_A = \frac{2}{e\varepsilon_0\varepsilon}\left(\frac{d\left(\frac{1}{C^2}\right)}{dV}\right)^{-1}$$

where C is capacitance of the space-charge layer. e, ε, ε_0 denote elementary charge, relative permittivity, vacuum permittivity. From slope of Mott–Schottky plots, the acceptor density of ZCO and ZnO/ZCO was found to be about 4.73×10^{18} cm^{-3} and 9.75×10^{20} cm^{-3}, respectively. The acceptor density of ZnO/ZCO is higher than that of ZCO. The more accumulation of holes at the interface of ZnO/ZCO sample can boost the electron transfer efficiency from analyte to electrode, resulting in improving electrochemical oxidation reactions towards analytes. Based on above-mentioned results, we have successfully synthesized $ZnO/ZnCo_2O_4$ heterojunction configuration with unique two-dimensional nanostructure assembled by uniform nanoparticles.

3.2. Cyclic voltammetric response of OFL and kinetic studies

Benefiting from the unique characteristics of heterojunction, the prepared ZnO/ZCO heterostructure was tested as an electrocatalyst for electrochemical sensing of OFL. The electrochemical response of OFL at different electrodes was first evaluated by cyclic voltammetry (CV) in 0.1 M PBS buffer solution. Fig. 4 a shows the CV curves of 100 μM OFL recorded on bare-SPE, ZCO/SPE, and ZnO/ZCO/SPE electrodes. All the CV curves exhibit a well-defined peak at 0.95–1.04 V assigned to the oxidation of OFL at electrode surface.[20,43] It is indicated that the mechanism of OFL electrochemical oxidation at electrode surface involved the oxidation of piperazine with two electrons and release of two protons, as shown in Scheme 1.[44] As expected, the ZnO/ZCO/SPE shows a significant enhancement of OFL electrochemical response compared to bare-SPE and ZCO/SPE. The OFL oxidation peak current is 1.6-fold and 1.3-fold higher than those of bare-SPE and ZCO/SPE, respectively (Fig. 4b). Moreover, the oxidation peak potential (E_p) shifts to more negative potential for ZCO (70 mV) and ZnO/ZCO (90 mV) electrodes. The increase in peak current response with peak potential shift suggest that the ZnO/ZCO heterostructures exhibit an excellent electrocatalytic activity for oxidation of OFL.[45]

As illustrated in Fig. 5a, the gradual increase of the oxidation peak current of OFL with increasing of scan rate in the range of 10 mV s^{-1} – 60 mV s^{-1} was observed. The oxidation peak current I_{pa} exhibits a linear relationship to $\nu^{1/2}$, with the fitted linear regression equation is $I_{pa} = 77.96\ \nu^{1/2} - 1.32$ ($R^2 = 0.999$), suggesting a diffusion-controlled processe of OFL oxidation on the ZnO/ZCO/SPE electrode (Fig. 5b). To confirm the OFL oxidation

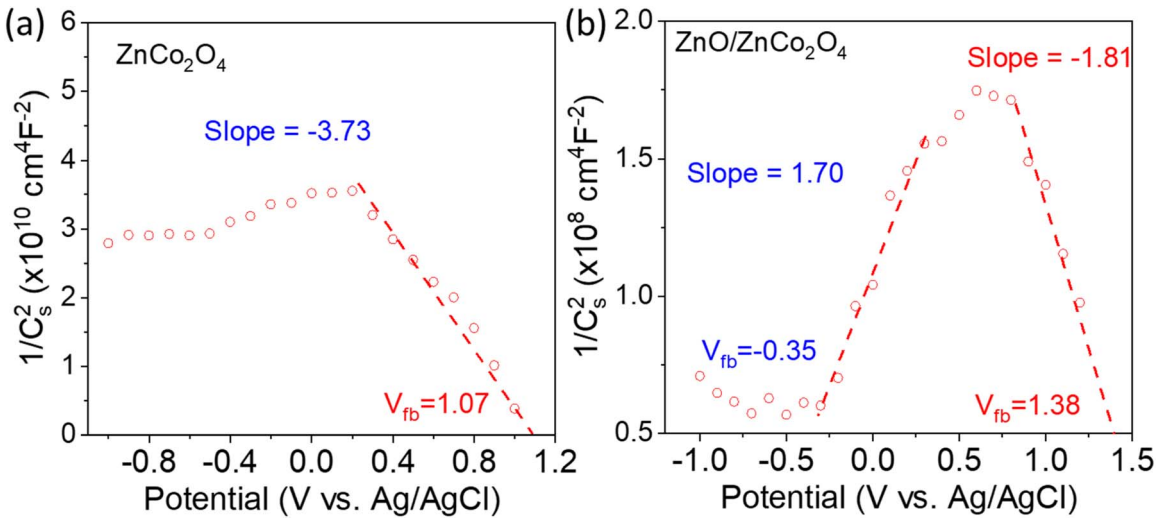

Fig. 3 The Mott–schottky plots of (a) $ZnCo_2O_4$ and (b) $ZnO/ZnCo_2O_4$ in 0.1 M Na_2SO_4.

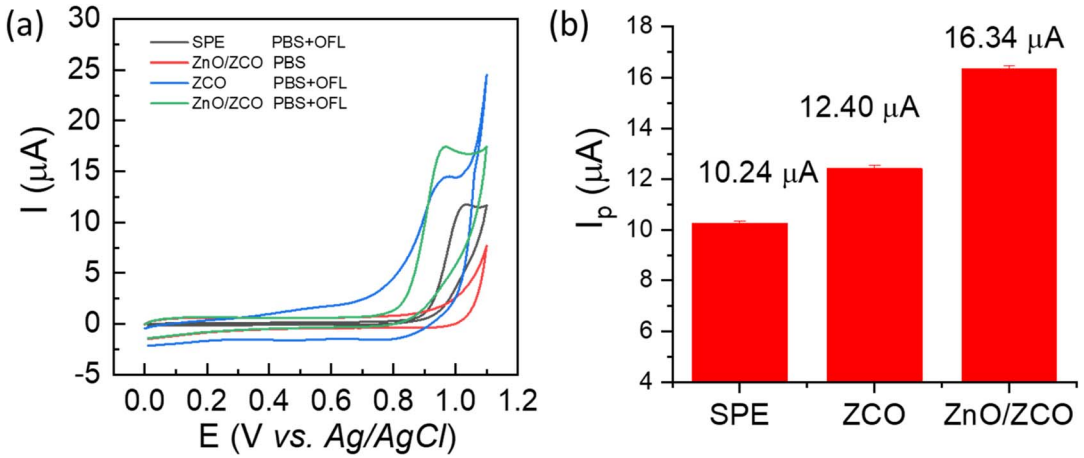

Fig. 4 (a) CV curves and (b) peak current response of 100 μM OFL recorded on bare SPE, ZCO/SPE and ZnO/ZCO/SPE in 0.1 M PBS (pH = 7.0).

mechanism, the linear relationship between $\log I_{pa}$ and $\log v$ was established. The obtained regression equation is: $\log I_{pa} = 0.56 \log v + 0.25$ ($R^2 = 0.999$) with a slope of 0.56, confirming a diffusion mechanism for the OFL electrochemical oxidation, as shown in Fig. 5c. In addition, a linear relationship of the oxidation peak potential (E_{pa}) and logarithm of scan rate ($\ln v$) is found with a corresponding linear equation: $E_{pa} = 0.031 \ln v + 0.843$. The proposed mechanism of electrochemical oxidation of ofloxacin with two protons and two electrons is further confirmed by the calculation results for the electron transfer number (n). The electron transfer number n is calculated to be about 1.66–2 by using following equation: slope $= RT/n(1-\alpha)F$.[46] Where, α is the transfer coefficient, and T, R, F denotes the standard implication.

To evaluate the electrocatalytic activity of heterostructure, chronoamperometry (CA) was carried out in 0.1 M PBS (pH = 7.0) in the absence and presence of 100 μM OFL, and the corresponding results are depicted in Fig. 6a and b. A linear relationship of I_{cat}/I_L and $t^{1/2}$ is observed with regression equations: $I_{cat}/I_L = 6.98\ t^{1/2} + 0.55$ with $R^2 = 0.98$ for ZnO/ZCO/SPE electrode, and $I_{cat}/I_L = 1.66t^{1/2} + 1.58$ with $R^2 = 0.98$ for ZCO/SPE electrode, respectively (Fig. 6c). Where I_L and I_{cat} denote the currents recorded on ZnO/ZCO/SPE and ZCO/SPE electrodes in the absence and presence of OFL, respectively. The catalytic rate constant (k_{cat}) is evaluated according to the method presented in the literature[47] using following equation:

$$I_{cat}/I_L = (\pi t)^{1/2}(k_{cat}C)^{1/2}$$

The catalytic rate constant is calculated to be 15.508 $\times 10^4$ $M^{-1}s^{-1}$ and 0.877 $\times$ 10^4 M^{-1} s^{-1} for ZnO/ZCO/SPE and ZCO/SPE electrodes, respectively. The k_{cat} of ZnO/ZCO/SPE is 17.68-fold higher than that of ZCO/SPE, indicating a superior electrocatalytic activity of ZnO/$ZnCo_2O_4$ heterostructures.

The diffusion coefficient (D_{OFL}) of OFL in solution is evaluated by using Cottrell's equation: $I = nFCAD^{1/2}(\pi t)^{-1/2}$, where C and D are the bulk concentration (mol cm^{-3}) and diffusion coefficient (cm^2 s^{-1}), n is number of electrons, and A is the electroactive surface area (EASA). Fig. 6d shows chronoamperograms for ZnO/$ZnCo_2O_4$/SPE in the presence of various OFL concentrations from 10 to 100 μM. The current I shows a linear relationship with $t^{-1/2}$ at long experimental times ($0.2 < t^{-1/2} < 0.5$), as depicted in Fig. 6e. The D_{OFL} value can be estimated from the linear relationship of slope and OFL concentration (Fig. 6f). The D_{OFL} value is calculated to be about 3.86 $\times$ 10^{-5} cm^2 s^{-1}.

To clarify the enhanced electrocatalytic activity, the electrochemical active surface area (EASA) and charge transfer resistance (R_{ct}) of bare-SPE, ZCO/SPE and ZnO/ZCO/SPE were investigated by using CV and EIS tests, and the obtained results are shown in Fig. S1 and S2. The calculation of EASA value and fitting the R_{ct} value are presented in the SI, and the obtained results are summarized in Table S3. The EASA value of ZCO/SPE (0.130 cm^2) and ZnO/ZCO/SPE (0.116 cm^2) was 2.9-fold and 2.6-fold greater than that of bare-SPE (0.045 cm^2), respectively. Interestingly, there is no significant difference in EASA value of ZnO/ZCO/SPE and ZCO/SPE, while R_{ct} value of ZnO/ZCO/SPE

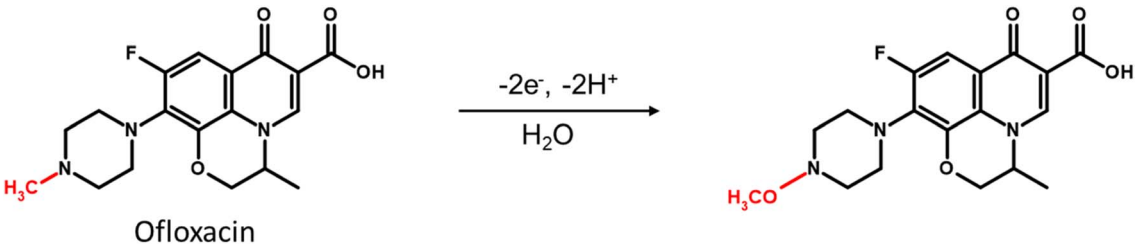

Scheme 1 The proposed oxidation mechanism of ofloxacin with two electrons and two protons.

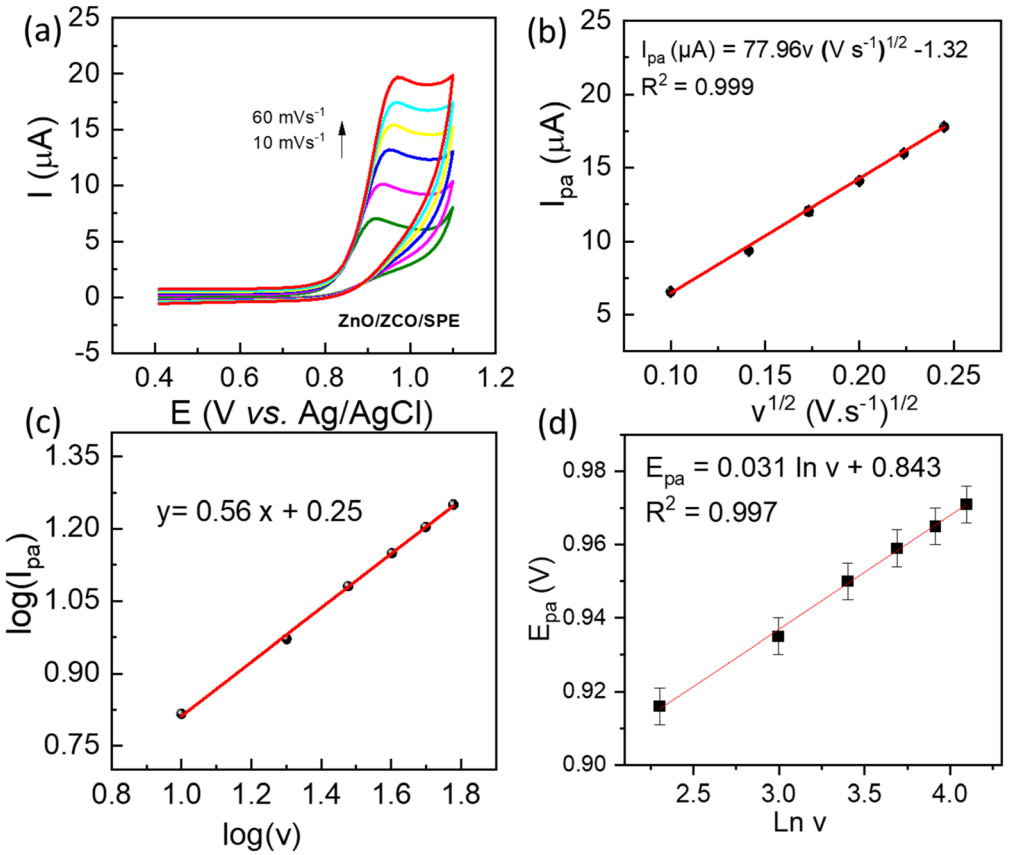

Fig. 5 (a) CV responses of 100 μM OFL on ZnO/ZCO/SPE in 0.1 M PBS (pH = 7.0) with different scan rates ranging from 10 mV s^{-1} to 60 mV s^{-1}, the corresponding calibration plots of (b) I_p *vs.* $v^{1/2}$; (c) log(I_p) *vs.* log(v); and (d) E_p *vs.* ln(v).

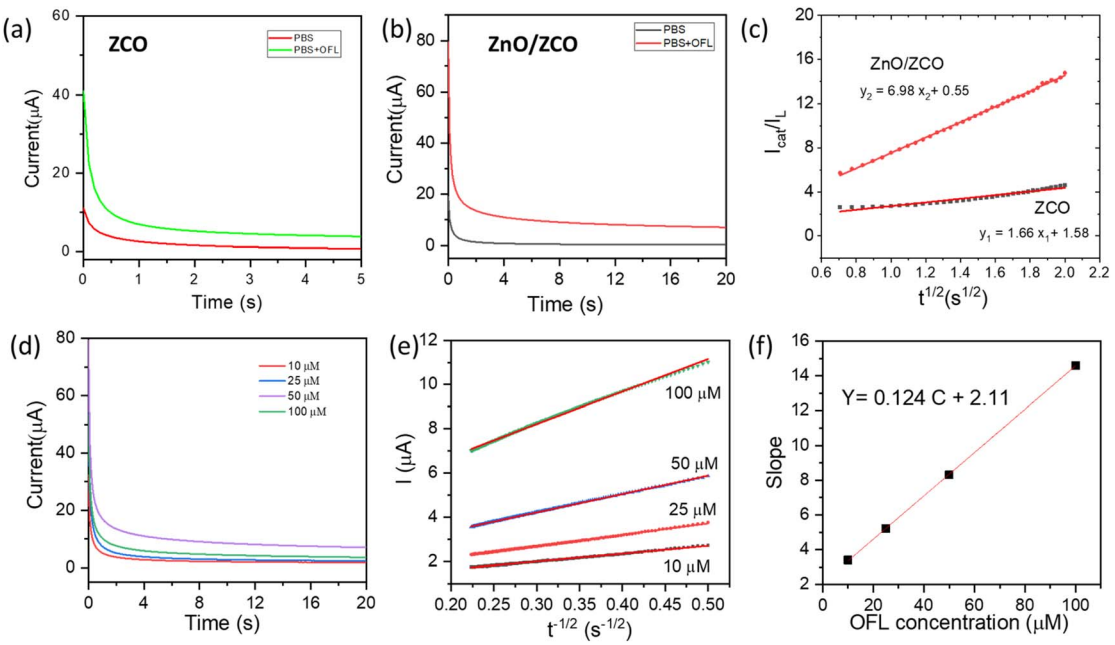

Fig. 6 Chronoamperograms for (a) ZCO/SPE and (b) ZnO/$ZnCo_2O_4$/SPE (20 s) in the absence and presence of 100 μM OFL, and (c) corresponding calibration plots of I_{cat}/I_L *vs.* $t^{1/2}$, (d) chronoamperograms for ZnO/ZCO/SPE in the presence of various OFL concentrations, (e) corresponding calibration plots of I *vs.* $t^{-1/2}$, (f) corresponding calibration plots of slope *vs.* OFL concentration.

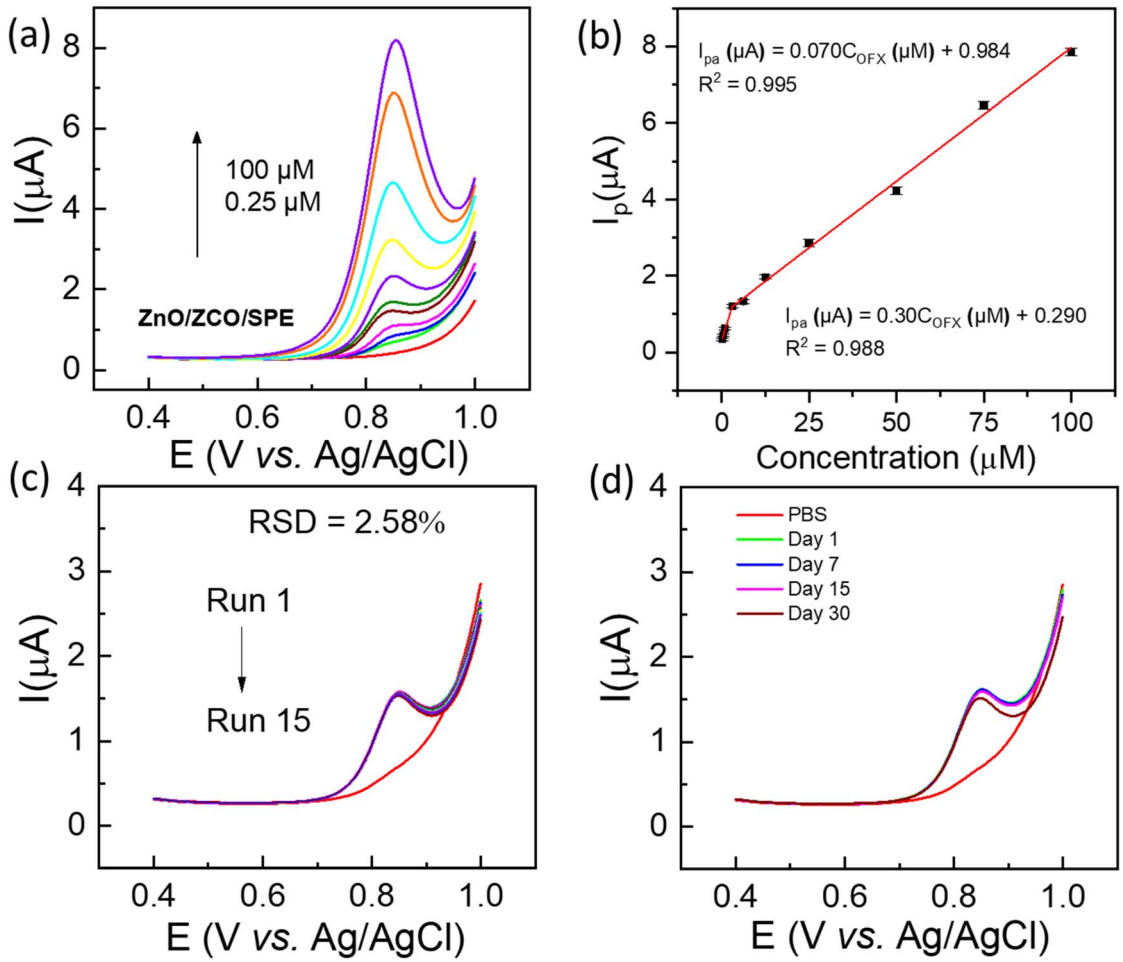

Fig. 7 (a) DPV curves recorded on the SPE electrode modified by ZnO/$ZnCo_2O_4$ heterostructures in 0.1 M PBS (pH = 4.0) containing different concentrations of OFL; (b) the corresponding calibration plot of I_{pa} and C_{OFL} with error bars; (c) DPV tests of 5 μM OFL with 15 consecutive runs in.0.1 PBS (pH = 4.0); (d) stability tests of ZnO/ZCO/SPE electrode.

(269.3 Ω) is 2.2-fold lower than that of ZCO/SPE (593.7 Ω). Moreover, the standard heterogeneous electron transfer rate constant (k_s) for electrochemical oxidation of OFL is determined by using Velasco's equation.[48]

$$k_s = 2.145 \exp\left(\frac{-0.02F}{RT}\right) D^{1/2} \left(E_p - E_{p/2}\right)^{-1/2} v^{1/2}$$

where, D is diffusion coefficient of OFL ($cm^2\ s^{-1}$), v is the scan rate ($V\ s^{-1}$), E_p and $E_{p/2}$ denote the peak potential and half-peak

Table 1 Comparison of ZnO/$ZnCo_2O_4$ heterostructures with various nanostructures for the electrochemical sensing of OFL[a]

Electrodes	Techniques	Linear ranges (μM)	LOD (nM)	Real samples	ref.
rGO/Pt–Au	DPV	0.08–100	50	Tablets and human urine samples	50
ZnO/GR/GCE	DPV	1–100	330	Pharmaceuticals	51
MW-CNTs/Nafion/GCE	LSV	0.5–100	100	Pharmaceuticals	52
GrO/CD/CPE	SWV	1–20	89	River water synthetic urine	53
Ag-CPE	DPV	4–1000	947	Tap water	54
Bi_2O_3/ZnO:f-MWCNT/GCE	DPV	0.5–39	30	Urine and serum samples	55
TAPB-TPA-COFs/PtNPs/GCE	CA	9.901×10^{-3}–1.406 2.024–15.19	2.184	Water	56
N-HCS/Fe3O4/GCE	DPV	0.096–40	28	Tap water and lake water	20
MoS_2@MWCNT/GCE	LSV	0.24–0.82	170	Rain, tap, and distilled water	57
	DPNV	0.29–0.82	120		
ZnO/$ZnCo_2O_4$/SPE	DPV	0.25–100	52	Tap water and lake water	This work

[a] Reduced graphene oxide (rGO); 1,3,5-tris(4-aminophenyl)benzene (TAPB) with terephthalaldehyde (TPA); covalent organic frameworks (COFs); N-doped hollow carbon spheres (N-HCS); multiwalled carbon nanotubes (MWCNT).

Table 2 Recovery report for detection test of OFL in environmental water and pharmaceutical samples

Sample	Added/ Labeled content (μM)	Found (μM)	Recovery (%)	RSD (%, $n = 3$)
Tap water	0.5	0.49	98.0	1.2
	10	9.86	98.6	2.5
	25	24.7	98.8	3.6
	50	49.6	99.2	3.6
Lake water	0.5	0.49	98.0	1.0
	10	9.88	98.8	3.2
	25	24.25	97.0	3.6
	50	49.22	98.4	4.8
Eye drop 1	10	10.22	102.2	3.0
Eye drop 2	10	10.51	105.1	1.7

potential (Fig. S3). The k_s value is calculated to be about 0.73 $cm^2\ s^{-1}$ and 1.13 $cm^2\ s^{-1}$ for ZCO/SPE and ZnO/ZCO/SPE, respectively. These results confirm that the improved electron transfer efficiency of heterostructures is decisive factor in contributing to the enhanced electrocatalytic activity of 2D ZnO/ZCO nanosheets.

3.3. Electrochemical sensing of OFL

The investigation of effect of pH electrolyte on the sensing properties was carried out to provide further information for redox mechanism of OFL, and optimize the analytical test conditions. The DPV curves of 100 μM OFL were recorded on the ZnO/ZCO/SPE in 0.1 M PBS solutions with various pH values, as illustrated in Fig. S4. It can be observed that the peak current response reaches the highest value at pH = 4 (Fig. S4). The result shows that the OFL electrochemical oxidation process involves gain and loss of proton. This can be attributed to the OFL molecules is accumulated on the ZnO/ZCO electrode surface primarily through combined hydrogen bonding and electrostatic forces. When pH value is less than pK_{a_1} of OFL (about 5.97), the OFL molecules are positively charged because of the amino group in the piperazine ring.[49] When pH value is greater than pK_{a1} and less pK_{a2} (7.9–8.2), the OFL molecules are uncharged because the carboxyl group on the OFL molecule loses a proton.[49] At pH = 4.0, the OFL molecules can be easily adsorbed to the surface of ZnO/ZCO, the highest value of peak current response is achieved. Thus, pH = 4.0 was selected for the subsequent tests. Moreover, there is the dependence of peak position (E_p) on the pH supporting electrolyte. The plot of E_p *vs.* pH indicates a linear relationship with regression equation of $E(V) = -0.03$ pH + 0.977. The obtained slope of 30 mV deviates significantly from the Nernst theoretical value (59 mV), implying an imbalance in the number of electrons and protons involved in the oxidation process of OFL.

Under optimized conditions, DPV voltammograms were recorded on the ZnO/ZCO/SPE electrode in 0.1 M PBS solution containing various concentrations of OFL. As depicted in Fig. 7a, the peak current gradually increases with the increase of OFL concentration from 0.25 to 100 μM. Fig. 7b shows linear relationship of peak current and OFL concentration with two different slopes, and the obtained regression equations are: I_{pa} (μA) = 0.300C_{OFL} (μM) + 0.290 with R^2 = 0.988 in the OFL concentration range from 0.25 μM to 6.25 μM and I_{pa} (μA) = 0.070C_{OFL} (μM) + 0.984 with R^2 = 0.995 in the range of 6.25–100 μM, respectively. From the slope of linear calibration with low OFL concentration, limit of detection (LOD) value was estimated to be 52 nM using the equation: LOD = 3SD/b, where SD and b denote the standard deviation of blank sample and slope

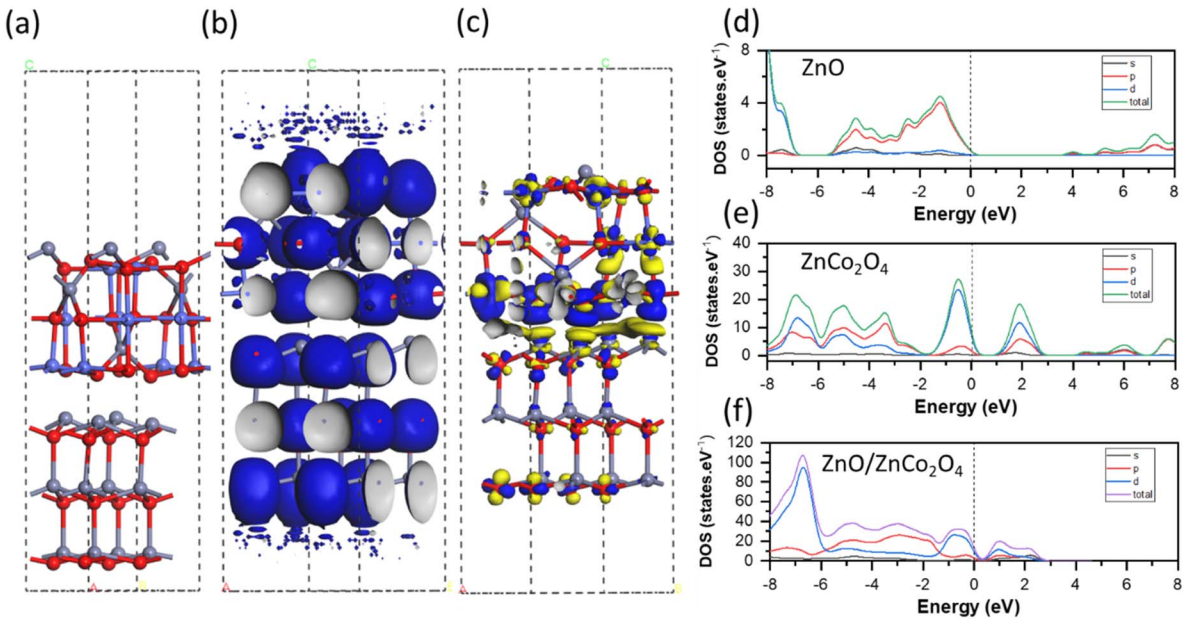

Fig. 8 (a) Lattice structure, (b) electron localization function, (c) iso-surface electron density differences (yellow: electron depletion and blue: electron accumulation) of the ZnO (001)/$ZnCo_2O_4$ (001) heterostructure, (d–f) the DOS of calculation of ZnO, $ZnCo_2O_4$, and ZnO/$ZnCo_2O_4$ heterostructures.

value. The electrochemical sensitivities were estimated to be 1.97 and 0.46 μA μM^{-1} cm^{-2} using the equation; $S = b/EASA$, with EASA denotes electrochemical active surface area. The higher slope value in the low OFL concentration range reveals that the ZnO/$ZnCo_2O_4$ heterojunction promotes efficient electron transfer kinetic through electrolyte/electrode interface. Owing to the high electrocatalytic activity of ZnO/$ZnCo_2O_4$ heterojunction, the OFL molecules on the modified electrode surface can be rapidly oxidized, resulting in a high sensitivity in the OFL concentration range from 0.25 μM to 6.25 μM. However, the reaction products may block the pores of the modified layers at high OFL concentrations, inducing a lower electrochemical sensitivity in the range of 6.25–100 μM. This is further confirmed by the CV response of OFL with various concentrations from 1 μM to 100 μM on the ZnO/$ZnCo_2O_4$ heterojunction. It is observed that the peak potential and half-peak potential of OFL shift to more positive potential towards the OFL concentrations in the range from 10 μM to 100 μM (Fig. S5). The obtained results suggest a slower electron transfer kinetics or mass transport limitations at high OFL concentrations. The sensing performance parameters of ZnO/$ZnCo_2O_4$ heterojunction and different nanostructures in the previous reports for detection of OFL is summarized in Table 1. The results revealed the ZnO/$ZnCo_2O_4$ heterojunction as a low cost and effective electrocatalyst for the monitoring of OFL in water.

3.4. Repeatability, reproducibility, and stability

The repeatability of ZnO/ZCO/SPE was evaluated by using the consecutive DPV measurements in the same conditions. Fig. 7c shows the DPV curves of 5 μM OFL in 0.1 M PBS with 15 consecutive runs. The obtained relative standard deviation (RSD) value was 2.58%, indicating the good repeatability of ZnO/ZCO/SPE. In addition, the reproducibility of ZnO/ZCO/SPE is also estimated by recording the peak current of five independent electrodes (Fig. S6a). The obtained result indicates an acceptable reproducibility of ZnO/ZCO/SPE with a RSD value of 3.60%. For long-term stability test, ZnO/ZCO/SPE electrode was stored at room temperature for detection of OFL. Fig. 7d shows the DPV curves of 5 μM OFL in 0.1 M PBS recorded on ZnO/ZCO/SPE electrode at different storage times. It can be seen that 93.8% of OFL peak current was retained after 30 days of storage at room temperature with an increase of RSD value to 5.2% for 6 consecutive runs.

3.5. Interference and real sample testing

To evaluate the anti-interference of ZnO/ZCO/SPE electrode, the analytical tests of OFL were carried out by adding the potential interfering compounds and ions, including: Mg^{2+}, Cu^{2+}, Co^{2+}, K^+, Na^+, PO_4^{2-}, SO_4^{2-}, Cl^-, acid ascorbic, glucose, chloramphenicol, paracetamol, furazolidone, and amoxicillin. As illustrated in Fig. S6b, it can be seen that the presence of 100-fold concentration of ions and 10-fold concentration of interfering compounds has a negligible effect on the detection of OFL. Therefore, it can be concluded that the ZnO/ZCO/SPE electrode can be used for the detection of OFL in environmental water samples.

To examine the feasibility of ZnO/ZCO/SPE electrode for detection of OFL in the environmental water samples and pharmaceutical samples, the analytical tests were conducted on lake water samples, tap water samples and eye drop samples. The environmental water samples were added with known concentrations of OFL, and DPV analysis were performed under optimized experiment conditions. It is worth emphasizing that the environmental water samples were analyzed without a pretreatment step. Fig. S7 shows the DPV curves of lake water and tap water samples recorded on ZnO/ZCO/SPE electrode. The test results were reported in Table 2. The recoveries were in the range of 97.0–98.8% for lake water, and from 98.0 to 99.2% for tap water, with the RSD values below 4.8%. For eye drop samples, the RSD values were lower than 3.0%, and recovery from 102.2 to 105.1%. These results demonstrate that the ZnO/$ZnCo_2O_4$-based electrochemical sensor is dependable for on-site analysis in real-water samples.

3.6. In-depth evaluation for ZnO/$ZnCo_2O_4$ heterostructure based on DFT calculations

The DFT calculations were conducted to validate the design concept of ZnO/$ZnCo_2O_4$ heterostructures and provide an insight for the enhanced electrocatalytic activity. As depicted in Fig. 8a, the crystalline structure of ZnO/$ZnCo_2O_4$ heterostructure was built using the ZnO (001) crystal plane and the $ZnCo_2O_4$ (001) crystal plane of with a mismatch of 13% for the DFT calculations. The electron localization function and charge density difference of ZnO/ZCO heterostructure is simulated to clarify the electron transfer process, as shown in Fig. 8(b and c). The electron localization function analysis indicates that the electrons mainly occur around O atoms, and some part of a covalent bond exists between Co and O atoms. The charge density difference results show a strong electron accumulation (blue region) on the interface side of $ZnCo_2O_4$, and whereas an electron depletion (yellow region) is near the ZnO side. This demonstrates that the electron transfer from ZnO to $ZnCo_2O_4$, resulting in the interfacial charge redistribution and a built-in electric field. The inner electric field can act as a driving force for interfacial electron transfer. Fig. 8(d–f) shows the TDOS and PDOS of ZnO, $ZnCo_2O_4$, and ZnO/$ZnCo_2O_4$ heterostructure. It is clear that the ZnO and $ZnCo_2O_4$ crystal structures possess a band gap to be about 2.960 and 1.144 eV, respectively. With the formation of the heterostructure, the PDOS in the ZnO/$ZnCo_2O_4$ heterostructure crosses the Fermi level (E_F), resulting in the higher electrical conductivity and lower interface electron transfer resistance for the heterojunctions compared to a single component.[32,36] Interestingly, ZnO/ZCO heterostructure shows a higher density of occupied electron states near the Fermi level compared to single phases. It can be observed that the Co d-orbital and O p-orbital are responsible for the PDOS near E_F of ZnO/ZCO heterostructure. The ZnO/ZCO heterostructure possesses a higher O p-orbital and Co d-orbital near Fermi level than that of ZnO or $ZnCo_2O_4$ arising from the increased hybridization between O p-orbital and Co d-orbital.[36] According to Marcus-Gerischer theory, the heterogeneous electron transfer rate depends on the DOS of electrode materials.[58] It has been reported earlier that the increase of DOS near E_F of electrode material

promotes the electron transfer across the interface of electrolyte/electrode.[59,60] Therefore, the formation of ZnO/ZCO heterojunction induces a significant increase of DOS near E_F, resulting in the faster electron transfer kinetics as compared to $ZnCo_2O_4$. These calculation results are in good agreement with the above-mentioned Mott–Schottky and CV analysis. The DFT calculation was carried out to provide insight into the interaction of OFL molecules with nanostructures. The geometries of adsorption configuration of OFL on the on the ZCO and ZnO/ZCO heterostructure are shown in Fig. S8, and adsorption energy (E_a) and distance between metal ion center and oxygen atom of electrocatalytic materials (ZCO and ZnO/ZCO) and atoms (O and H) of OFL are documented in Table S4. The ZnO/ZCO heterostructure shows E_a value of −20.51 kcal mol^{-1} which is larger absolute value of adsorption energy of OFL on the ZCO (−15.06 kcal mol^{-1}). The OFL molecules adsorbed on the ZCO surface through the O atom and H atom with the O–Co and H–O distances are 2.865 and 2.815 Å, respectively. For ZnO/ZCO heterostructure surface, the OFL molecules interact with O atom and Zn atom of $ZnCo_2O_4$ surface with the O–Zn and H–O distances are 2.752 and 2.841 Å, respectively. With the formation of ZnO/ZCO heterostructure, Zn atoms act a crucial role in the interaction of OFL molecules with $ZnCo_2O_4$ surface. These results suggest that the surface charge redistribution can affect the adsorption capacity of OFL on electrocatalyst material. The experimental and DFT calculation results confirm that constructing the ZnO/ZCO heterostructure allows the interfacial charge redistribution and a built-in electric field formation, which promote the interfacial electron transfer and electrocatalytic activity to achieve excellent electrochemical performance in the detection of OFL.

4. Conclusion

In summary, this study proposes a rapid synthesis method of ZnO/$ZnCo_2O_4$ heterostructures *via* microwave-assisted hydrothermal technique. The ZnO/$ZnCo_2O_4$ heterostructures with 2D nanosheet structure exhibited an excellent electrocatalytic activity towards ofloxacin with a 17.68-fold increase in catalytic rate constant value as compared to single $ZnCo_2O_4$. The p–n heterojunction configuration with internal electric field promoted electron transfer efficiency, leading to enhanced electrocatalytic activity towards ofloxacin. The ZnO/$ZnCo_2O_4$ nanosheets-based electrochemical sensor provided a high electrochemical sensitivity in linear range of 0.25–100 μM and limit of detection reached to 52 nM. The proposed sensor also exhibits a good stability and good anti-interference with the addition of interference substances. The reliability of ZnO/ZCO/SPE has been verified in actual water samples and pharmaceutical samples with a good recovery rate of 97.0–105.1%. The present study recommends that the ZnO/$ZnCo_2O_4$ heterostructures can be useful for the affordable electrochemical sensing of antibiotics with enhanced performance.

Author contributions

V. T. H. Mai: methodology, validation, investigation; N. N. Huyen: validation, investigation, formal analysis; N. T. Vinh: formal analysis, writing—original draft; L. M. Tung: methodology, validation; T. V. Hoang: methodology, formal analysis; P. M. Huong: methodology, formal analysis, writing—review & editing; Anh-Tuan Le: conceptualization, methodology, supervision, writing—review & editing, project administration; N. X. Dinh: conceptualization, methodology, formal analysis, writing—review & editing.

Conflicts of interest

The authors declare that they have no known competing financial interests or personal relationships that could have appeared to influence the work reported in this paper.

Data availability

Data will be made available on request.

Supplementary information (SI) is available. See DOI: https://doi.org/10.1039/d5ra08937a.

Acknowledgements

This work was supported by Phenikaa University (grant number PU2023-1-A-21). The authors also thank the NEB Lab (Phenikaa University) for UV-vis spectra, Raman spectra, and Electrochemical measurements.

References

1 S. S. Sambaza and N. Naicker, Contribution of wastewater to antimicrobial resistance: A review article, *J. Glob Antimicrob Resist*, 2023, **34**, 23–29, DOI: 10.1016/j.jgar.2023.05.010.
2 K. Watanabe, K. Numata-Watanabe and S. Hayasaka, Methicillin-resistant staphylococci and ofloxacin-resistant bacteria from clinically healthy conjunctivas, *Ophthalmic Res.*, 2001, **33**, 136–139.
3 E. Hapeshi, A. Achilleos, M. I. Vasquez, C. Michael, N. P. Xekoukoulotakis, D. Mantzavinos and D. Kassinos, Drugs degrading photocatalytically: kinetics and mechanisms of ofloxacin and atenolol removal on titania suspensions, *Water Res.*, 2010, **44**, 1737–1746.
4 K. Sato, Y. Matsuura, M. Inoue, T. Une, Y. Osada, H. Ogawa and S. Mitsuhashi, In vitro and in vivo activity of DL-8280, a new oxazine derivative, *Antimicrob. Agents Chemother.*, 1982, **22**, 548–553.
5 J. P. Monk and D. M. Campoli-Richards, Ofloxacin, *Drugs*, 1987, **33**, 346–391.
6 K. Mitani and H. Kataoka, Determination of fluoroquinolones in environmental waters by in-tube solid-phase microextraction coupled with liquid chromatography–tandem mass spectrometry, *Anal. Chim. Acta*, 2006, **562**, 16–22, DOI: 10.1016/j.aca.2006.01.053.
7 L. A. Shervington, M. Abba, B. Hussain and J. Donnelly, The simultaneous separation and determination of five quinolone antibotics using isocratic reversed-phase HPLC: Application to stability studies on an ofloxacin tablet formulation, *J. Pharm. Biomed. Anal.*, 2005, **39**, 769–775.

8 C. Fierens, S. Hillaert and W. Van den Bossche, The qualitative and quantitative determination of quinolones of first and second generation by capillary electrophoresis, *J. Pharm. Biomed. Anal.*, 2000, **22**, 763–772, DOI: 10.1016/S0731-7085(99)00282-4.

9 T. T. T. Tran, M. N. Do, T. N. H. Dang, Q. H. Tran, V. T. Le, A. Q. Dao and Y. Vasseghian, A state-of-the-art review on graphene-based nanomaterials to determine antibiotics by electrochemical techniques, *Environ. Res.*, 2022, **208**, 112744, DOI: 10.1016/j.envres.2022.112744.

10 E. Dezhakam, M. Tavakkol, T. Kafili, E. Nozohouri, A. Naseri, B. Khalilzadeh and R. Rahbarghazi, Electrochemical and optical (bio)sensors for analysis of antibiotic residuals, *Food Chem.*, 2024, **439**, 138145, DOI: 10.1016/j.foodchem.2023.138145.

11 K. Rudnicki, K. Sipa, M. Brycht, P. Borgul, S. Skrzypek and L. Poltorak, Electrochemical sensing of fluoroquinolone antibiotics, *TrAC, Trends Anal. Chem.*, 2020, **128**, 115907, DOI: 10.1016/j.trac.2020.115907.

12 A. Joshi and K.-H. Kim, Recent advances in nanomaterial-based electrochemical detection of antibiotics: Challenges and future perspectives, *Biosens. Bioelectron.*, 2020, **153**, 112046, DOI: 10.1016/j.bios.2020.112046.

13 X. Li, Z.-Y. Zhang and F. Li, Flexible electrochemical sensors based on nanomaterials: Constructions, applications and prospects, *Chem. Eng. J.*, 2025, **504**, 158101, DOI: 10.1016/j.cej.2024.158101.

14 S. Chen, J. Guo, Q. Sun, Y. Wang, M. Du, A. Wang, X. Yu and L. Ding, Enhanced electrochemical sensor based on Uio-66-NH2/carbon nanotubes hybrid for selective detection of ofloxacin, *Mater. Today Chem.*, 2024, **42**, 102441, DOI: 10.1016/j.mtchem.2024.102441.

15 M. Taherizadeh, S. Jahani, M. Moradalizadeh and M. M. Foroughi, Synthesis of a dual-functional terbium doped copper oxide nanoflowers for high-efficiently electrochemical sensing of ofloxacin, pefloxacin and gatifloxacin, *Talanta*, 2023, **255**, 124216, DOI: 10.1016/j.talanta.2022.124216.

16 A. Wong, T. A. Silva, F. C. Vicentini and O. Fatibello-Filho, Electrochemical sensor based on graphene oxide and ionic liquid for ofloxacin determination at nanomolar levels, *Talanta*, 2016, **161**, 333–341, DOI: 10.1016/j.talanta.2016.08.035.

17 J. M. Gonçalves, L. V. de Faria, A. B. Nascimento, R. L. Germscheidt, S. Patra, L. P. Hernández-Saravia, J. A. Bonacin, R. A. A. Munoz and L. Angnes, Sensing performances of spinel ferrites MFe2O4 (M = Mg, Ni, Co, Mn, Cu and Zn) based electrochemical sensors: A review, *Anal. Chim. Acta*, 2022, **1233**, 340362, DOI: 10.1016/j.aca.2022.340362.

18 J. M. Gonçalves, D. P. Rocha, M. N. T. Silva, P. R. Martins, E. Nossol, L. Angnes, C. S. Rout and R. A. A. Munoz, Feasible strategies to promote the sensing performances of spinel MCo 2 O 4 (M = Ni, Fe, Mn, Cu and Zn) based electrochemical sensors: a review, *J. Mater. Chem. C*, 2021, **9**, 7852–7887, DOI: 10.1039/D1TC01550H.

19 N. Solangi, J. Kumar, G. Naz and R. A. Soomro, The preparation of NiCo2O4 nanoboulders and their application in the electrochemical detection of ofloxacin drug, *JCIS Open*, 2022, **6**, 100054, DOI: 10.1016/j.jciso.2022.100054.

20 D. Liao, R. Wang, Y. Zheng, J. Ma, J. Sun, Q. Yang and G. Zhou, In-situ growth of small-size Fe3O4 nanoparticles on N-doped hollow carbon spheres for electrochemical high-efficiency determination of ofloxacin-contaminated water, *Microchem. J.*, 2023, **191**, 108927, DOI: 10.1016/j.microc.2023.108927.

21 J. S. de Castro, A. V. Chaves, P. B. A. Fechine, R. C. de Oliveira, F. W. P. Ribeiro, P. de Lima-Neto, D. S. Abreu, C. L. C. G. de Oliveira and A. N. Correia, Electrocatalytic Amplified Sensor For Determination of Ofloxacin Using Zn 2 SnO 4/Reduced Graphene Oxide Composite As Surface-Modifying Agent, *J. Electrochem. Soc.*, 2024, **171**, 017501, DOI: 10.1149/1945-7111/ad1633.

22 H. Shu, T. Lai, B. Yao, M. Li, H. Li, S. Wang, T. Chen, X. Xiao and Y. Wang, Synergistic effect between p–n heterojunction and oxygen vacancies of Co3O4-C/Fe-MOF for highly sensitive detection of trace atrazine, *Chem. Eng. J.*, 2024, **490**, 151652, DOI: 10.1016/j.cej.2024.151652.

23 J. Zhang, H. Jiang, J. Gao, C. Zhao and H. Suo, Three-dimensional CeO2 Nanosheets/CuO nanoflowers p–n heterostructure supported on carbon cloth as electrochemical sensor for sensitive nitrite detection, *Anal. Chim. Acta*, 2025, **1336**, 343526, DOI: 10.1016/j.aca.2024.343526.

24 F. Zhou, H. Zhao, Z. Shi, J. Hou and M. Lan, The first principle calculation of heterojunction based on CuO-CeO2 and its application in electrochemical detection of dopamine and tyrosine, *Chem. Eng. J.*, 2025, **522**, 167701, DOI: 10.1016/j.cej.2025.167701.

25 X. H. Chen, J. Y. Ren, N. B. Li and H. Q. Luo, Constructing of CoP-Nb2O5 p–n heterojunction with built-in electric field to accelerate the charge migration in electrocatalytic hydrogen evolution, *J. Colloid Interface Sci.*, 2023, **651**, 760–768, DOI: 10.1016/j.jcis.2023.08.032.

26 J. Zhao, A. B. M. Ali, A. A. H. Kadhum, H. Lin, A. S. Abdelhameed, A. M. Alanazi, I. Mahariq, E. Khudoynazarov, D. Jumanazarov and F. Atamurotov, Boosting photocatalytic H2O2 production and non-biodegradable ofloxacin removal via a novel Ti3C2 MXene nanosheet-supported BiVO4/InVO4 Z-scheme heterojunction: Optimization and mechanism insights, *J. Water Process. Eng.*, 2025, **74**, 107722, DOI: 10.1016/j.jwpe.2025.107722.

27 X. Song, P. Chen, S. Huang and K. Xiao, A highly sensitive photoelectrochemical aptasensor based on CdS/Cu2MoS4 heterojunction coupled with PdPtAu MNs nanozyme for the detection of ofloxacin in water environment, *Microchem. J.*, 2025, **216**, 114606, DOI: 10.1016/j.microc.2025.114606.

28 J. Zhang, S. Cui, Y. Ding, X. Yang, K. Guo and J.-T. Zhao, Two-dimensional mesoporous ZnCo2O4 nanosheets as a novel electrocatalyst for detection of o-nitrophenol and p-

nitrophenol, *Biosens. Bioelectron.*, 2018, **112**, 177–185, DOI: 10.1016/j.bios.2018.03.021.

29 N. N. Huyen, L. M. Tung, T. A. Nguyen, T. L. Huong Phung, P. D. Thang, N. T. Vinh, Q. Van Nguyen, T. K. Oanh Vu, V. D. Lam, V. K. Le, N. X. Dinh and A.-T. Le, Insights into the Effect of Cation Distribution at Tetrahedral Sites in ZnCo 2 O 4 Spinel Nanostructures on the Charge Transfer Ability and Electrocatalytic Activity toward Ultrasensitive Detection of Carbaryl Pesticide in Fruit and Vegetable Samples, *J. Phys. Chem. C*, 2023, **127**, 12262–12275, DOI: 10.1021/acs.jpcc.3c02039.

30 M. Natesan and Y.-C. Chen, Temperature-driven phase engineering of spinel ZnCo2O4 catalyst for sensitive detection of fungicide in environmental sample, *Appl. Surf. Sci.*, 2025, **714**, 164368, DOI: 10.1016/j.apsusc.2025.164368.

31 N. P. Shetti, S. D. Bukkitgar, K. R. Reddy, C. V. Reddy and T. M. Aminabhavi, ZnO-based nanostructured electrodes for electrochemical sensors and biosensors in biomedical applications, *Biosens. Bioelectron.*, 2019, **141**, 111417, DOI: 10.1016/j.bios.2019.111417.

32 H. Zhang, X. Zhou, Y. Liu, B. Hou, L. Ma, Y. Liu, H. Liu, S. Zhang, Z. Ao, J. Song, J. Wang and X. Zhao, Delicate fabrication of ZnO/ZnCo 2 O 4 heterojunction HoMSs as anodes for lithium-ion batteries with high rate capability, *Mater. Chem. Front.*, 2022, **6**, 3318–3328, DOI: 10.1039/D2QM00688J.

33 H. Zhu, H. Ji, R. Zhang, Z. Mu, Y. Liu, Z. Yuan, Y. Shen and F. Meng, Ppb-level butanone sensor based on porous spherical ZnCo2O4/ZnO through the synergy effects of Co2+ atoms and unique wrinkled structure, *Sens. Actuators B Chem.*, 2023, **393**, 134087, DOI: 10.1016/j.snb.2023.134087.

34 N. C. Junior, Y. Du, Y. Wang, G. Zhao, J. Li, A. Riaz and J. Du, Self-assembled aggregates of SnO2/Bi2O3 heterojunction for electrochemical H2O2 detection, *J. Environ. Chem. Eng.*, 2025, **13**, 116260, DOI: 10.1016/j.jece.2025.116260.

35 P. Wang, W. Shen, Q. Zhang, M. Li, A. Fan, W. Ma, L. Li, J. Gao, F. Wu, D. Geng and W. Hu, Orbital Hybridized MoO 3/MoSe 2 Heterojunction for Dual-Driven Interfacial Reaction and Charge Transfer Toward Enhanced Electrochemical Response, *ACS Nano*, 2025, **19**, 35562–35574, DOI: 10.1021/acsnano.5c10076.

36 Q. Ma, F. Cui, J. Zhang and T. Cui, Built-in electric field boosted ionic transport kinetics in the heterostructured ZnCo2O4/ZnO nanobelts for high-performance supercapacitor, *J. Colloid Interface Sci.*, 2023, **629**, 649–659, DOI: 10.1016/j.jcis.2022.09.013.

37 H. Ma, X. Wu, X. Li, J. Liu, H. Dong, Y. Liu, L. Niu, F. Zhang, W. Wang, C. Shao, X. Li and Y. Liu, Photocatalytic CO 2 Reduction to Ethanol by ZnCo 2 O 4/ZnO Janus Hollow Nanofibers, *Inorg. Chem.*, 2024, **63**, 15735–15751, DOI: 10.1021/acs.inorgchem.4c01643.

38 W. Wang, Facile hydrothermal synthesis of ZnCo 2 O 4 nanostructures : controlled morphology and magnetic properties, *J. Mater. Sci.:Mater. Electron.*, 2021, **32**, 16662–16668, DOI: 10.1007/s10854-021-06221-w.

39 M. Šćepanović, M. Grujić-Brojčin, K. Vojisavljević, S. Bernik and T. Srećković, Raman study of structural disorder in ZnO nanopowders, *J. Raman Spectrosc.*, 2010, **41**, 914–921, DOI: 10.1002/jrs.2546.

40 S. Lu, H. Wang, J. Zhou, X. Wu and W. Qin, Atomic layer deposition of ZnO on carbon black as nanostructured anode materials for high-performance lithium-ion batteries, *Nanoscale*, 2017, **9**, 1184–1192, DOI: 10.1039/C6NR07868K.

41 Y. Ding, J. Zhang, Y. Yang, L. Long, L. Yang, L. Yan, W. Kong, F. Liu, F. Lv and J. Liu, Fully-depleted dual P–N heterojunction with type-II band alignment and matched build-in electric field for high-efficient photocatalytic hydrogen production, *Int. J. Hydrogen Energy*, 2021, **46**, 36069–36079, DOI: 10.1016/j.ijhydene.2021.08.175.

42 W.-Y. Zhou, J.-Y. Liu, J.-Y. Song, J.-J. Li, J.-H. Liu and X.-J. Huang, Surface-Electronic-State-Modulated, Single-Crystalline (001) TiO 2 Nanosheets for Sensitive Electrochemical Sensing of Heavy-Metal Ions, *Anal. Chem.*, 2017, **89**, 3386–3394, DOI: 10.1021/acs.analchem.6b04023.

43 R. Liu, X. Zhang, T. Wu, R. Liu, W. Cui, Y. Sun and B. Ren, Development of a molecularly imprinted Ag/g-C3N4/GCE electrochemical sensor for specific detection of ofloxacin, *Colloids Surf. A Physicochem. Eng. Asp.*, 2024, **700**, 134679, DOI: 10.1016/j.colsurfa.2024.134679.

44 H. Han, J. Li and X. Pang, Electrochemical Sensor Using Glassy Carbon Electrode Modified with HPMαFP/Ppy/GCE Compos ite Film for Determination of Ofloxacin, *Int. J. Electrochem. Sci.*, 2013, **8**, 9060–9070, DOI: 10.1016/S1452-3981(23)12949-X.

45 M. Zhen, Y. Wang, C. Xu, Y. Yi, J. Huang, L. Li and T. You, Dual-enhanced electrochemiluminescence of Au nanoclusters: Ag doping-induced emission and Ce-MOFs-induced excitation, *Biosens. Bioelectron.*, 2025, **288**, 117833, DOI: 10.1016/j.bios.2025.117833.

46 E. Laviron, General expression of the linear potential sweep voltammogram in the case of diffusionless electrochemical systems, *J. Electroanal. Chem. Interfacial Electrochem.*, 1979, **101**, 19–28, DOI: 10.1016/S0022-0728(79)80075-3.

47 M. Pournaghi-Azar and R. Sabzi, Electrochemical characteristics of a cobalt pentacyanonitrosylferrate film on a modified glassy carbon electrode and its catalytic effect on the electrooxidation of hydrazine, *J. Electroanal. Chem.*, 2003, **543**, 115–125, DOI: 10.1016/S0022-0728(02)01480-8.

48 J. G. Velasco, Determination of standard rate constants for electrochemical irreversible processes from linear sweep voltammograms, *Electroanalysis*, 1997, **9**, 880–882, DOI: 10.1002/elan.1140091116.

49 Z. Liu, Q. Wang, Q. Xue, C. Chang, R. Wang, Y. Liu and H. Xie, Highly efficient detection of ofloxacin in water by samarium oxide and β-cyclodextrin-modified laser-induced graphene electrode, *Microchem. J.*, 2023, **186**, 108353, DOI: 10.1016/j.microc.2022.108353.

50 Z. Jiang, Q. Liu, Y. Tang and M. Zhang, Electrochemical Sensor Based on a Novel Pt–Au Bimetallic Nanoclusters Decorated on Reduced Graphene Oxide for Sensitive Detection of Ofloxacin, *Electroanalysis*, 2017, **29**, 602–608, DOI: 10.1002/elan.201600408.

51 X. Si, Y. Wei, C. Wang, L. Li and Y. Ding, A sensitive electrochemical sensor for ofloxacin based on a graphene/zinc oxide composite film, *Anal. Methods*, 2018, **10**, 1961–1967, DOI: 10.1039/c8ay00127h.

52 K. Huang, X. Liu, W. Xie and H. Yuan, Voltammetric behavior of ofloxacin and its determination using a multi-walled carbon nanotubes-Nafion film coated electrode, *Microchim. Acta*, 2008, **162**, 227–233, DOI: 10.1007/s00604-008-0943-z.

53 A. M. Santos, A. Wong, F. C. Vicentini and O. Fatibello-Filho, Simultaneous voltammetric sensing of levodopa, piroxicam, ofloxacin and methocarbamol using a carbon paste electrode modified with graphite oxide and β-cyclodextrin, *Microchim. Acta*, 2019, **186**, 1–9, DOI: 10.1007/s00604-019-3296-x.

54 K. Elaslani, A. Loudiki, B. Chhaibi, F. Laghrib, S. El Houssame, M. Bakasse, S. Lahrich, A. Farahi and M. A. E. L. Mhammedi, Enhancing of ofloxacin oxidation current through the overvoltage position displacement using carbon paste electrode modi fi ed by silver particles : Analytical application in water, *Chem. Inorg. Mater.*, 2023, **1**, 100013, DOI: 10.1016/j.cinorg.2023.100013.

55 N. Manjula, T.-W. Chen, S.-M. Chen and B.-S. Lou, Sonochemical Synthesis and Characterization of Rod-Shaped Bi 2 O 3/ZnO Anchored with f-MWCNT Nanocomposite for the Electrochemical Determination of Ofloxacin, *J. Electrochem. Soc.*, 2021, **168**, 087506, DOI: 10.1149/1945-7111/ac1891.

56 J. Hao, L. Huang, L. Zheng, Q. Wang, Z. Yin, H. Li, L. Jia, W. Liao and K. Liu, A direct electrochemical sensor based on covalent organic frameworks/platinum nanoparticles for the detection of ofloxacin in water, *Microchim. Acta*, 2024, **191**, 145, DOI: 10.1007/s00604-024-06205-7.

57 R. Sharma, S. Kumar, D. S. Rana, S. Thakur, N. Gupta and D. Singh, Molybdenum disulfide nanostructure grown on multi-walled carbon nanotube for the electrochemical detection of ofloxacin, *J. Environ. Chem. Eng.*, 2024, **12**, 112413, DOI: 10.1016/j.jece.2024.112413.

58 R. Memming, Electron Transfer Theories, in:*Semicond. Electrochem.*, Wiley, 2015, pp. 127–168, DOI: 10.1002/9783527688685.ch6.

59 V. A. Kislenko, S. V. Pavlov and S. A. Kislenko, Influence of defects in graphene on electron transfer kinetics: The role of the surface electronic structure, *Electrochim. Acta*, 2020, **341**, 136011, DOI: 10.1016/j.electacta.2020.136011.

60 S. Roy, S. Singh, M. Khan, E. Chamanehpour, S. Sain, T. Goswami, S. S. Roy, Y. K. Mishra and A. Mathur, Electrochemistry at 2D and 3D nanoelectrodes: The interplay between interface kinetics and surface density of states, *Electrochim. Acta*, 2024, **477**, 143762, DOI: 10.1016/j.electacta.2024.143762.